



Crystallographically vacancy-induced MOF nanosheet as rational single-atom support for accelerating CO₂ electroreduction to CO

Jin Hyuk Cho¹ | Joonhee Ma¹ | Chaehyeon Lee² | Jin Wook Lim³ |
 Youngho Kim¹ | Ho Yeon Jang² | Jaehyun Kim⁴ | Myung-gi Seo⁵ |
 Youngeon Choi⁵ | Youn Jeong Jang⁶ | Sang Hyun Ahn⁷ | Ho Won Jang⁴  |
 Seoin Back² | Jong-Lam Lee³ | Soo Young Kim¹ 

¹Department of Materials Science and Engineering, Korea University, Seoul, Republic of Korea

²Department of Chemical and Biomolecular Engineering, Sogang University, Seoul, Republic of Korea

³Department of Materials Science and Engineering, Pohang University of Science and Technology (POSTECH), Pohang, Republic of Korea

⁴Department of Materials Science and Engineering, Research Institute of Advanced Materials, Seoul National University, Seoul, Republic of Korea

⁵Lotte Chemical R&D Center, Daejeon, Republic of Korea

⁶Department of Chemical Engineering, Hanyang University, Seoul, Republic of Korea

⁷School of Chemical Engineering and Material Science, Chung-Ang University, Seoul, Republic of Korea

Correspondence

Seoin Back, Department of Chemical and Biomolecular Engineering, Institute of Emergent Materials, Sogang University, 04107 Seoul, Republic of Korea.

Email: sback@sogang.ac.kr

Jong-Lam Lee, Department of Materials Science and Engineering, Pohang University of Science and Technology (POSTECH), 790-784 Pohang, Republic of Korea.

Email: jilee@postech.ac.kr

Soo Young Kim, Department of Materials Science and Engineering, Korea University, 02841 Seoul, Republic of Korea.

Email: sooyoungkim@korea.ac.kr

Funding information

National Research Foundation of Korea (NRF), Grant/Award Numbers: 2021R1A4A3027878, RS-2023-00209139, 2015M3D3A1A01064929; Korea Institute

Abstract

To attain a circular carbon economy and resolve CO₂ electroreduction technology obstacles, single-atom catalysts (SACs) have emerged as a logical option for electrocatalysis because of their extraordinary catalytic activity. Among SACs, metal–organic frameworks (MOFs) have been recognized as promising support materials because of their exceptional ability to prevent metal aggregation. This study shows that atomically dispersed Ni single atoms on a precisely engineered MOF nanosheet display a high Faradaic efficiency of approximately 100% for CO formation in H-cell and three-compartment microfluidic flow-cell reactors and an excellent turnover frequency of 23,699 h⁻¹, validating their intrinsic catalytic potential. These results suggest that crystallographic variations affect the abundant vacancy sites on the MOF nanosheets, which are linked to the evaporation of Zn-containing organic linkers during pyrolysis. Furthermore, using X-ray absorption spectroscopy and density functional theory calculations, a comprehensive investigation of the unsaturated atomic coordination environments and the underlying

Jin Hyuk Cho, Joonhee Ma, and Chaehyeon Lee contributed equally.

This is an open access article under the terms of the [Creative Commons Attribution](https://creativecommons.org/licenses/by/4.0/) License, which permits use, distribution and reproduction in any medium, provided the original work is properly cited.

© 2024 The Authors. *Carbon Energy* published by Wenzhou University and John Wiley & Sons Australia, Ltd.

of Energy Technology & Energy (MOTIE) of the Republic of Korea, Grant/Award Number: 20212010100040

mechanism involving CO* preadsorbed sites as initial states was possible and provided valuable insights.

KEYWORDS

2-dimensional material, carbon dioxide reduction, metal-organic frameworks, single-atom catalysts, vacancy sites

1 | INTRODUCTION

The electrochemical reduction of carbon dioxide (eCO₂RR) is a cutting-edge method for achieving carbon neutrality that has attracted substantial attention.^{1–3} However, this reaction is limited in terms of high overpotential, low conversion efficiency, the inevitable hydrogen evolution reaction (HER), and sluggish stability. Moreover, the thermodynamic stability and robust C=O bonds of CO₂ molecules challenge their activation.^{4–6} These obstacles impede electron and proton transfer during the eCO₂RR. Therefore, rational electrocatalysts that can create highly active catalytic sites while ensuring long-term stability must be investigated.^{7–9} Single-atom catalysts (SACs) differ from traditional catalysts because they use isolated metal atoms anchored on support materials as active sites, enabling nearly 100% efficiency in metal atom utilization.^{10,11} Despite their exceptional advantages, single-metal atoms agglomerate into nanoparticles due to their high surface energies, producing inferior activity.¹² Therefore, appropriate SAC supports are required to prevent excessive aggregation and stabilize single atoms. Among the diverse support materials, zeolitic imidazolate frameworks, a subclass of metal-organic frameworks (MOFs) with high nitrogen content, have been extensively used to prepare metal-nitrogen-doped carbon SACs with dense active sites.^{13–15} This study used an eco-friendly approach to design two-dimensional (2D) ZIF-8 nanosheets (ZIF-8-NSs) as optimal support materials for SACs. The Ni precursor was added during the synthesis of ZIF-8-NS (Ni-ZIF-8-NS), which underwent pyrolysis at 950°C under an N₂ atmosphere, resulting in the final product, Ni-NC-NS. Following a comprehensive investigation using experimental and theoretical approaches, the generation of vacancy sites in the synthesized materials depended on their crystallographic characteristics. The atomic coordination of Ni-NC-NS, comprising one Ni single atom combined with two N atoms and two vacancy sites (NiN₂-V₂), was revealed using synchrotron radiation-based X-ray absorption spectroscopy (XAS). Ni-NC-NS demonstrated excellent eCO₂RR performance, exhibiting a high Faradaic CO₂-to-CO conversion efficiency (FE_{CO}) of approximately 100% in H-cell and flow-cell reactors and a remarkable turnover frequency (TOF) of 23,699 h⁻¹. Density functional theory (DFT) calculations were performed using CO* preadsorbed sites (CO*) as the

initial states and applying the d-band theory for an in-depth theoretical study to determine the mechanisms responsible for the superior electrocatalytic performance of the catalysts.

2 | EXPERIMENTAL SECTION

2.1 | Preparation of the electrocatalysts

Bimetallic Zn/Ni ZIF-8-NSs were prepared using a solution synthesis method. A Zn(NO₃)₂·6H₂O (0.297 g) and Ni(NO₃)₂·6H₂O (0.099 g) solution in 45 mL of deionized (DI) water was added to a 2-methylimidazole (1 g) solution in 45 mL of DI water. After stirring for 24 h at room temperature, the precipitates were centrifuged (3500 rpm, 10 min), washed twice with DI water, and dried at 80°C for 24 h. Subsequently, the sample was placed in a tube furnace and heated at 950°C for 4 h (heating rate of 2°C min⁻¹) under an N₂ atmosphere to obtain Ni-NC-NS. The same solution synthesis method adopted for Ni-ZIF-8-NS was also utilized to prepare bimetallic Zn/Ni ZIF-8 particles (labeled Ni-ZIF-8-P); however, different solvents were used. A 200 mL methanol solution of Zn(NO₃)₂·6H₂O (2.97 g) and Ni(NO₃)₂·6H₂O (1.2 g) was mixed with another 200 mL methanol solution of 2-methylimidazole (6.85 g). After stirring for 24 h at room temperature, the precipitate was centrifuged (3500 rpm, 10 min), washed twice with methanol, and dried at 80°C for 24 h. Afterward, the sample was placed in a tube furnace and heated at 950°C for 4 h (heating rate of 2°C min⁻¹) under an N₂ atmosphere to yield Ni-NC-P. NC-NS and NC-P electrocatalysts were constructed using the same solution synthesis method employed for Ni-ZIF-8-NS and Ni-ZIF-8-P without adding the Ni precursor. Subsequently, the resulting samples were heated using a tube furnace at 950°C for 4 h (heating rate of 2°C min⁻¹) under an N₂ atmosphere.

2.2 | Material characterizations

The morphologies and sizes of the samples were determined using field-emission scanning electron

microscopy (SEM; Sigma, ZEISS). High-resolution transmission electron microscopy (TEM) images were acquired using a JEM-2100F microscope (JEOL), and the corresponding element maps were obtained using energy-dispersive spectrometry (EDS; Oxford Instruments). Aberration-corrected high-angle annular dark-field scanning TEM (HAADF-STEM) images were obtained using a Cs-corrected TEM (Themis Z 60-300; Thermo Fisher Scientific) operating at 200 kV. The Ni-NC-NS and Ni-NC-P samples were deposited on a Cu mesh TEM grid to acquire TEM images. The X-ray diffraction (XRD) patterns were collected using a Bruker New D8-Advance diffractometer with a Cu K α radiation X-ray source. X-ray photoelectron spectroscopy (XPS) was performed using a ULVAC-PHI X-TOOL instrument with Al K α as the X-ray source. Inductively coupled plasma atomic emission spectroscopy (ICP-AES; OPTIMA 4300DV; PerkinElmer) was conducted using Ar plasma as the source to confirm atom loading on the as-prepared samples. The specific surface area and porosity were quantified using the Brunauer-Emmett-Teller (BET; ASAP2020) equation based on the N₂ adsorption/desorption isotherms. To confirm the presence of a vacancy site in materials, electron paramagnetic resonance (EPR) spectroscopy was carried out at 273 K (Bruker EMX/Plus spectrometer). XAS was performed in transmittance and fluorescence detection modes at beamline 8D at the Pohang Accelerator Laboratory. The XAS data, including X-ray absorption near-edge spectroscopy (XANES) and extended X-ray absorption fine structure (EXAFS) data, were analyzed using the ATHENA and ARTEMIS programs of the IFEFFIT package.

2.3 | Electrode preparation and electrochemical measurements

The method described for electrode preparation was applied to all the investigated samples. To prepare the working electrode for the eCO₂RR, 5 mg as-prepared catalyst powder and 5 mg carbon black were dispersed in 1 mL ethanol and 40 μ L Nafion solution (5 wt%) and sonicated for 2 h. Subsequently, 20 μ L of the homogeneous catalyst ink was drop-cast onto a 1 \times 1 cm² polytetrafluoroethylene (PTFE)-treated carbon paper (Sigracet 39 BB) and dried at room temperature. Electrochemical experiments were performed in a customized H-type cell separated into cathodic and anodic sections using a Nafion membrane (212; Dupont Co.). A standard three-electrode system (working, counter, and reference electrodes)

was used. eCO₂RR was performed in the cathodic section, which comprised the working electrode (1 \times 1 cm²) and reference electrode (saturated calomel electrode [SCE]) in 20 mL CO₂-purged 0.5 M KHCO₃ at pH 7.2. The anodic section comprised a Pt mesh counter electrode in 20 mL Ar-purged 0.5 M KHCO₃ at pH 8.8. Throughout the electrochemical measurements, 20 mL min⁻¹ CO₂ gas was used as the electrolyte in the cathodic section. The SCE reference electrode was converted into a reversible hydrogen electrode (RHE) scale as follows:

$$E(\text{vs. RHE}) = E(\text{vs. SCE}) + 0.222 \text{ V} + 0.0592 \times \text{pH}. \quad (1)$$

Linear sweep voltammetry (LSV) polarization curves were obtained at a scan rate of 10 mV s⁻¹. The CO and H₂ gas products during the eCO₂RR were detected using online gas chromatography (GC; 7890 B; Agilent Technologies). CO and H₂ were detected using a flame ionization detector (FID) and a thermal conductivity detector (TCD), respectively. The liquid products were analyzed using nuclear magnetic resonance (NMR; VNS6000 MHz) spectroscopy with dimethyl sulfoxide as the internal standard. No liquid products were detected in the NMR spectra. Electrochemical surface area (ECSA) was calculated as follows:

$$\text{ECSA} = \frac{C_{\text{dl}}}{C_s}, \quad (2)$$

where C_{dl} and C_s are the double-layer and specific capacitances, respectively. The average C_s was 50 μ F cm⁻² throughout the area at scan rates of 10, 20, 40, 60, 80, and 100 mV s⁻¹, the potential window of 0.6–0.85 V versus RHE, and the mass of the catalyst (5 mg) in a CO₂-purged 0.5 M KHCO₃ electrolyte. The C_{dl} at 0.725 V versus RHE was estimated as follows:

$$C_{\text{dl}} = \frac{\Delta j}{2} (\Delta j = j_a - j_c). \quad (3)$$

To conduct the experiments in a flow-cell reactor, the catalyst ink was spray-coated onto PTFE-treated carbon paper measuring 1 \times 1 cm² and dried at room temperature. Catalyst loading was maintained at 3 mg cm⁻². In both electrolytes, 0.5 M KHCO₃ and 1 M KOH were cycled through each compartment at 50 mL min⁻¹. The CO₂ gas was introduced into the system at 100 mL min⁻¹.

To evaluate the selectivity of the electrocatalysts, the FE_{CO} was calculated as follows:

$$FE_{CO}(\%) = \frac{j_{CO}}{j_{total}} = \frac{v_{CO}zF}{j_{total}}, \quad (4)$$

where FE_{CO} is the Faradaic efficiency for CO production, %; j_{CO} is the partial current density of CO; j_{total} is the total current density; v_{CO} is the concentration of CO, mol, as measured using GC; z is the number of electrons exchanged for product formation; $Z=2$ for CO and H_2 , F is the Faradaic constant ($F=96,485 \text{ C mol}^{-1}$),

To quantify the intrinsic electroactivity, the TOF was calculated as follows:

$$TOF(h^{-1}) = \frac{j_{CO}/zF}{m_{cat} \times (m_{Ni}/M_{Ni})} \times 3600, \quad (5)$$

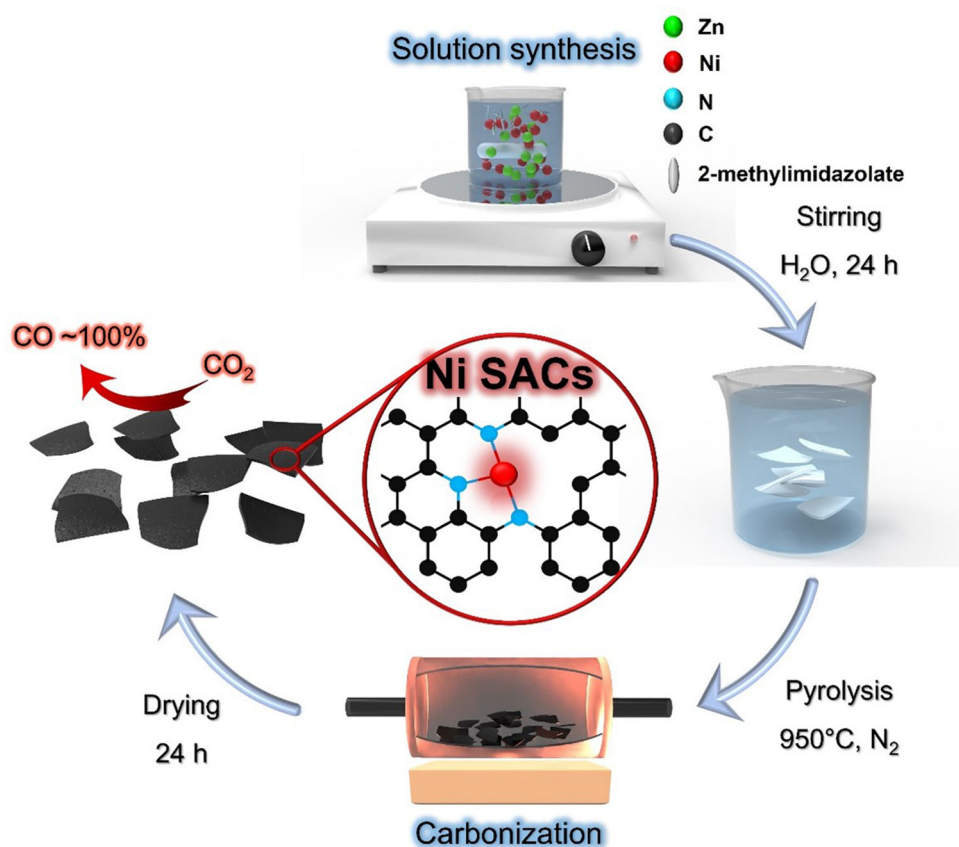
j_{CO} is the partial current density of CO (j_{CO} values of Ni-NC-NS are 18.1, 22.5, and 26.8 mA cm^{-2} at -1.0 , -1.1 , and -1.2 V vs. RHE , respectively). z is the number of electrons exchanged for product formation (two for CO, $z=2$). F is the Faradaic constant ($F=96,485 \text{ C mol}^{-1}$). m_{cat} is the catalyst mass on the electrode ($m_{cat}=0.2 \text{ mg cm}^{-2}$). m_{Ni} is the Ni metal loading of the catalyst (Ni-NC-NS: 0.6 wt% obtained using ICP-AES).

M_{Ni} is the atomic mass of the transition metal ($M_{Ni}=58.6934 \text{ g mol}^{-1}$).

3 | RESULTS AND DISCUSSION

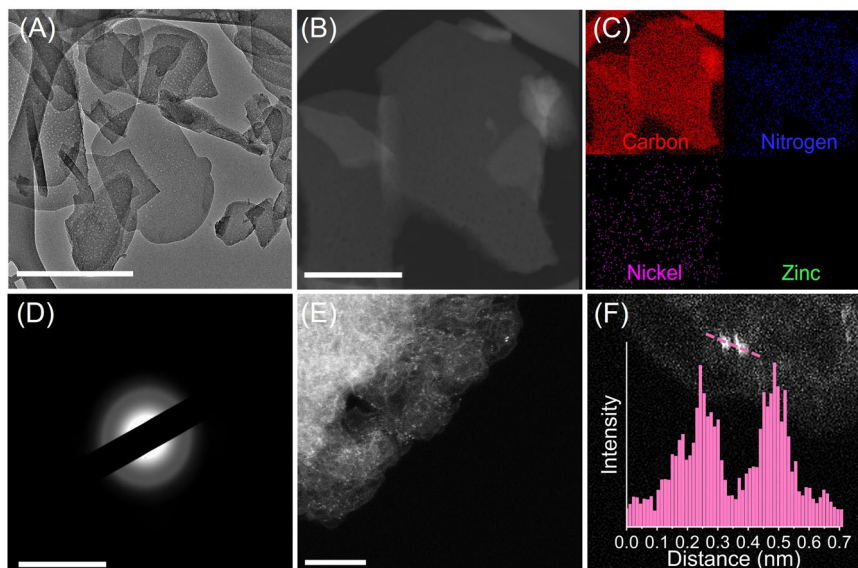
3.1 | Catalyst synthesis and characterization

Scheme 1 illustrates the fabrication process for dispersed single Ni atoms anchored on ZIF-8-NS. Initially, Zn (NO_3)₂ and Ni(NO_3)₂ metal sources, 2-methylimidazole organic ligands, and DI water were mixed and stirred for 24 h at room temperature to synthesize Ni-ZIF-8-NS. The final Ni-NC-NS product was obtained via high-temperature pyrolysis for carbonization. However, traditional 3D Ni-ZIF-8-P and its pyrolyzed products (Ni-NC-P) were synthesized using methanol, a toxic solvent. SEM and TEM images of Ni-NC-NS revealed a nanosheet structure with an average area of approximately 300 nm (Figures 1A and S1), comparable to those of ZIF-8-NS and Ni-ZIF-8-NS (Figure S2). Additionally, HAADF-TEM images with the corresponding EDS



SCHEME 1 Schematic of the synthesis method and proposed vacancy-manipulated Ni-N_x active site architecture of Ni-NC-NS.

FIGURE 1 Morphological characterizations of the Ni-NC-NS catalyst. (A) TEM image (scale bar = 400 nm), (B) HAADF-TEM image (scale bar = 200 nm), (C) corresponding elemental mapping profiles for C, N, Ni, and Zn elements obtained using EDS elemental mapping (red, blue, pink, and green colors represent C, N, Ni, and Zn, respectively), (D) SAED pattern (scale bar = 10 nm^{-1}), (E) HAADF-STEM image (scale bar = 5 nm), and (F) magnified aberration-corrected HAADF-STEM image of Ni-NC-NS. Inset in (F) shows the line profiles of Ni single atoms obtained from the pink dotted line.



mapping profiles confirmed well-dispersed Ni, N, and C in the porous graphitic carbon nanosheet structure; however, no Zn signals were detected (Figure 1B,C). The ring-like selected-area electron diffraction (SAED) pattern demonstrates the crystallinity of Ni-NC-NS, exhibiting a diffraction pattern of amorphous carbon (Figure 1D).¹⁶ Aberration-corrected HAADF-STEM images at different atomic magnifications showed isolated, dense bright spots representing single Ni atoms anchored on the graphitic carbon nanosheet structure (Figure 1E,F). Line profile analysis confirmed that the signal intensity associated with a single Ni atom was distinguishable (Figure 1F). Atomic force microscopy revealed a thickness of approximately 5 nm for Ni-ZIF-8-NS, indicating that thin nanosheets can offer abundant exposure sites (Figure S3).¹⁷ Ni-NC-P exhibited hexagonal facets with an average size of approximately 60 nm and a single Ni atom insertion on the ZIF-8-P support (Figure S4). However, Zn was detected in the EDS mapping, distinguishing it from Ni-NC-NS. The digital photographs of the samples before and after pyrolysis are shown in Figure S5.

The crystal structures of the fabricated materials were examined using XRD. The results show that ZIF-8-NS has a monoclinic crystal structure, with Zn^{2+} cations coordinated to four nitrogen atoms from the imidazolate group (Figure S6).¹⁸ In contrast, ZIF-8-P exhibits the typical cubic crystal structure of ZIF-8.¹⁹ These differences in crystal structures are attributed to the polar environment and symmetry of the molecular structure, which depend on the solvent used.²⁰ Furthermore, no significant changes in the peaks of ZIF-8-P and ZIF-8-NS were observed after adding Ni ions. The simulated and experimental XRD patterns

were compared to confirm the monoclinic and cubic crystal structures of ZIF-8-NS and ZIF-8-P, respectively (Figure S7). Optimized monoclinic ZIF-8-NS and cubic ZIF-8-P crystal structures were obtained (Figure S8). After high-temperature pyrolysis at 950°C , broad carbon diffraction patterns were observed in the XRD patterns of all as-prepared samples at 25° and 44° , assigned to the (002) and (100) planes, respectively (Figure 2A). The XRD analysis showed no characteristic peaks of metallic Zn (JCPDS No. 900-8522) or Ni (JCPDS No. 004-0850), indicating that single Ni atoms were dispersed effectively on the graphitic carbon support, thereby preventing metal aggregation.²¹ The Raman spectra indicated that Ni-NC-NS had a higher peak intensity ratio (1.06) of D band and G band (I_D/I_G) than Ni-NC-P (0.97), suggesting that Ni-NC-NS has a larger number of defective sites, a rich vacancy environment, and disordered carbon sites due to Zn evaporation (Zn boiling point: 907°C ; Figure 2B).²² However, a slight decrease in the I_D/I_G ratio was observed after adding Ni (Figure S9). To support the findings from the Raman measurements, we further conducted EPR spectroscopy experiments to confirm the presence of vacant sites by observing a magnetic signal in g-values. A distinctive isotopic EPR signal emerged at $g = 2.004$, revealing that the carbon atoms within Ni-NC-NS, which possess abundant nitrogen vacancy sites, induce magnetism (Figure S10).²³ XPS was used to examine the chemical compositions and valence states. The XPS survey spectra of Ni-NC-NS and Ni-NC-P show the presence of Ni, N, O, and C (Figure 2C); however, only Ni-NC-P contains Zn, consistent with the EDS results (Table S1). The high-resolution XPS spectrum of N 1s exhibited the

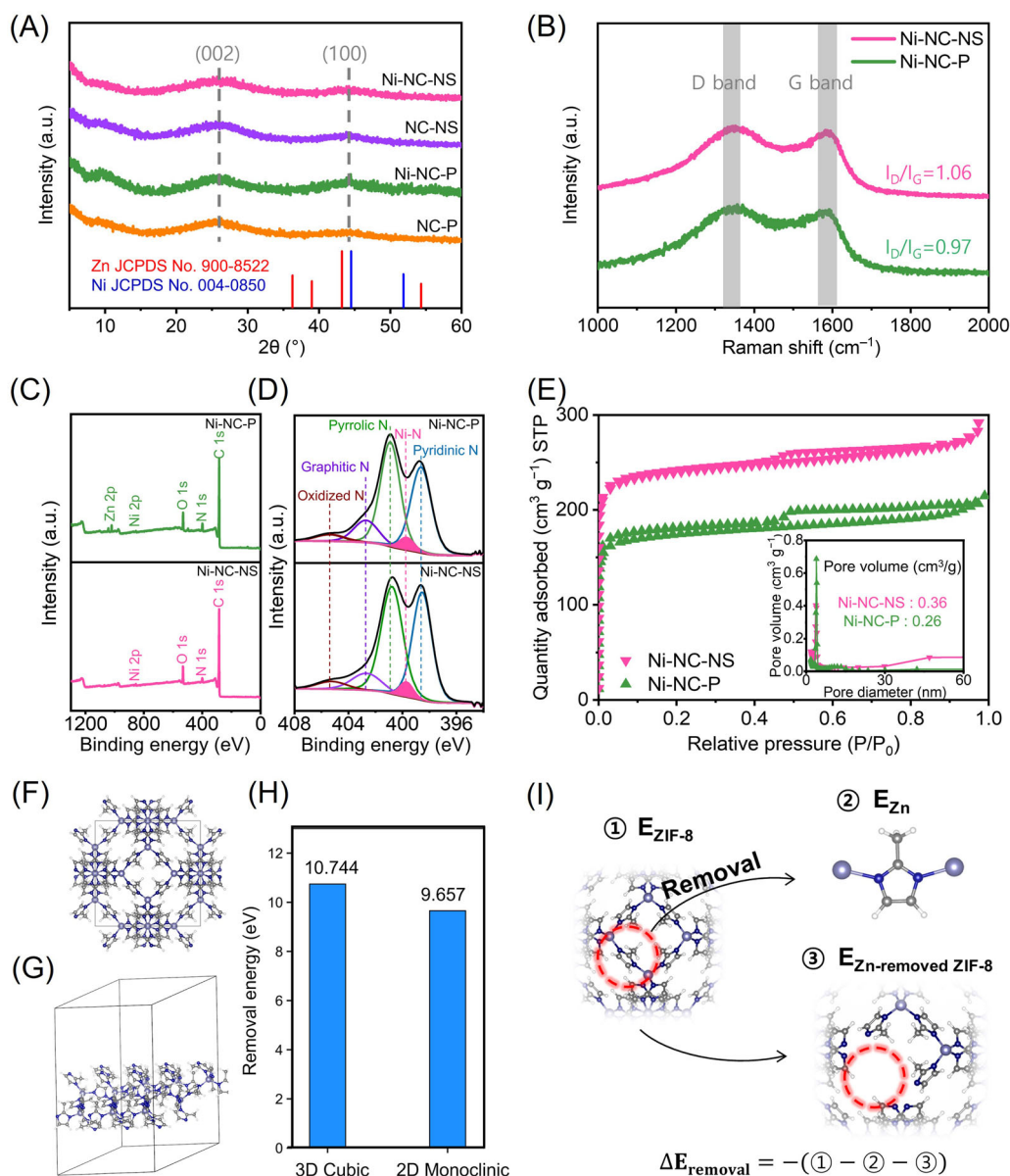


FIGURE 2 Characteristic analysis of materials. (A) XRD patterns of NC-P, Ni-NC-P, NC-NS, and Ni-NC-NS for crystal structure. The JCPDS profiles of metallic Zn (red) and Ni (blue) are represented. (B) Raman spectra, (C) XPS survey spectra, (D) N 1s high-resolution XPS spectra, and (E) BET analysis of Ni-NC-P and Ni-NC-NS (inset shows average pore size distributions of Ni-NC-P and Ni-NC-NS). Optimized atomic structure models of (F) cubic ZIF-8-P and (G) monoclinic ZIF-8-NS. (H) Computed removal energies of the Zn-containing organic linker from each structure. (I) Schematic of the removal energy calculation procedure for materials.

deconvolution of Ni-NC-NS and Ni-NC-P into five different N configurations, namely pyridinic N, Ni-N, pyrrolic N, graphitic N, and oxidized N, with binding energies of 398.2, 399.5, 400.5, 401.3, and 403.4 eV, respectively. These configurations facilitated the formation of rich anchor sites to stabilize the Ni metal centers (Figure 2D).^{24,25} Additionally, high-resolution XPS spectra of Ni 2p_{3/2} for Ni-NC-NS and Ni-NC-P showed peaks between the Ni foil (Ni⁰; 853.5 eV) and Ni²⁺ (855.8 eV), highlighting the oxidative Ni^{δ+} nature of Ni (0 < δ < 2; Figure S11).²⁶ N₂ adsorption and

desorption isotherms were obtained using the BET method to investigate the specific surface area and pore structure. The results demonstrated that Ni-NC-NS had a total pore volume of 0.36 cm³ g⁻¹, a mesoporous structure, and a specific surface area of 930 m² g⁻¹, which was significantly higher than that of Ni-NC-P (688 m² g⁻¹; Figure 2E). The corresponding pore size distribution diagram shows micropores and mesopores in Ni-NC-NS.²⁷ Therefore, the exceptional advantages of Ni-NC-NS, including its remarkably high specific surface area and abundant porosity, are

attributed to its extensive exposure to active sites during catalytic reactions.²⁸

3.2 | Investigation of a vacancy-manipulated site

XPS was conducted on Ni-ZIF-8-NS at various pyrolysis temperatures for 4 h to investigate the effects of vacancies resulting from the evaporation of Zn. As the pyrolysis temperature increased from 750°C to 950°C, there was a noticeable decrease in Zn content from 2.47% to 1.39% to 0% (Figure S12, region A), confirming complete Zn evaporation at 950°C while retaining Ni (Figure S12, region B). Furthermore, XPS measurements of NC-NS and NC-P, including survey spectra and elemental analysis, revealed Zn only in NC-P (Figure S13 and Table S2). Residual Zn was still detected in NC-P and Ni-NC-P, even after pyrolysis at 1000°C for 10 h. To investigate the thermal stability and decomposition properties of the catalysts with various crystal structures, thermogravimetric analysis (TGA) was conducted under an N₂ atmosphere (Figure S14). Initially, cubic Ni-ZIF-8-P exhibited a significant mass loss between the initial (T_i) and final mass loss temperatures (T_f) at 439°C and 557°C, respectively, indicating a disintegrated crystal structure and degraded organic components (Figure S14A).²⁹ The T_i of monoclinic Ni-ZIF-8-NS was comparable to that of cubic Ni-ZIF-8-P, while the T_f was more than 85°C lower than that of cubic Ni-ZIF-8-P (Figure S14B). Based on this phenomenon, it was hypothesized that monoclinic Ni-ZIF-8-NS decomposes the CN fragments containing Zn at an earlier stage than that of cubic Ni-ZIF-8-P, thereby allocating additional energy to residual Zn evaporation, porphyrin structural stabilization, and vacancy manipulation.²⁹ Additional investigations were conducted to substantiate the abovementioned analyses and hypotheses. First, the removal energy ($\Delta E_{\text{removal}}$) of 2-methylimidazolate Zn-containing organic linker from ZIF-8 was calculated: $\Delta E_{\text{removal}} = -(\Delta E_{\text{ZIF-8}} - \Delta E_{\text{Zn}} - \Delta E_{\text{Zn-removed ZIF-8}})$, where a more positive $\Delta E_{\text{removal}}$ indicates a higher energy requirement for removal, thus indicating a sluggish removal process of the Zn-containing organic linker. The atomic structures of cubic ZIF-8-P and monoclinic ZIF-8-NS were analyzed to determine the energy required for removal (Figure 2F,G). The calculated $\Delta E_{\text{removal}}$ indicated that it was easier to remove the Zn-containing organic linker from monoclinic ZIF-8-NS (9.66 eV) than from cubic ZIF-8-P (10.74 eV; Figure 2H,I). Due to its significantly lower removal energy, monoclinic ZIF-8-NS exhibited complete Zn evaporation during high-temperature pyrolysis. This prevented metal aggregation, stabilized the porphyrin

structure, and induced a more abundant vacancy environment. Conversely, the residual Zn in Ni-NC-P required higher energy barriers than those of Ni-NC-NS for CO₂ activation to form COOH* in the eCO₂RR system, which can be attributed to the coordinatively unsaturated environment.³⁰

3.3 | In-depth investigation of atomic environments

XAS was used to investigate the local structural and electronic properties of single Ni atoms in Ni-NC-NS at the atomic level. Ni K-edge XANES showed that the Ni-NC-NS was situated between Ni⁰ and Ni phthalocyanine (NiPc) (Ni²⁺) (Figure 3A). This result indicates that the valence state of isolated Ni atoms is in the Ni^{δ+} nature range ($0 < \delta < 2$), consistent with the XPS results. Fourier-transform EXAFS (FT-EXAFS) spectroscopy was performed to investigate the atomic environment of Ni-NC-NS at the Ni K-edge. The major peak of Ni-NC-NS was identified at approximately 1.33 Å (Figure 3B) and assigned to the first shell. This suggests a significantly shorter Ni-N interaction than the Ni-N coordination peak of NiPc (1.44 Å). Additional insights into the various atomic environments, such as the coordination number (CN) and precise Ni-N bond distance, were obtained through FT-EXAFS curve fitting, which consistently exhibited positive values in the magnitude R space ($|\chi(R)|$) at the Ni K-edge (Figure 3C). Subsequently, FT-EXAFS in the real R space ($\text{Re}[\chi(R)]$), which oscillates between positive and negative values, was performed to verify the reliability of the data (Inset in Figure 3C). EXAFS curve fitting analyses demonstrated that the CN of Ni species in Ni-NC-NS was 2.3 ± 0.1 , revealing the configuration of most NiN₂-V₂ (NiN_{*x*}-V_{*y*}, where N and V indicate the nitrogen and vacancy, respectively, and x and y indicate their respective CNs). In addition, FT-EXAFS in real q space ($\text{Re}[\chi(q)]$) was transformed back into the wavevector space (the window function was assigned in q space at 0–8 Å⁻¹), indicating well-matched and well-fitted data (Figure 3D).³¹ The Ni-N configuration in Ni-NC-NS was discerned via 2D representative wavelet-transformed-EXAFS, encompassing k and R spaces (Figure S15). Additional XAS analyses were performed, including fitting the EXAFS curves of the Ni foil, NiPc, and Ni-ZIF-8-NS (Figure S16). The XAS analysis revealed that Ni-NC-P exhibited a Ni^{δ+} ($0 < \delta < 2$) valence state at the Ni K-edge. The CN of Ni-NC-P was 3.2 ± 0.2 , and the prominent peak was observed at approximately 1.39 Å, indicating a longer Ni-N bond length than that of Ni-NC-NS (Figure S17A–C). Table S3 shows the Ni K-edge EXAFS curve-fitting results for the reference

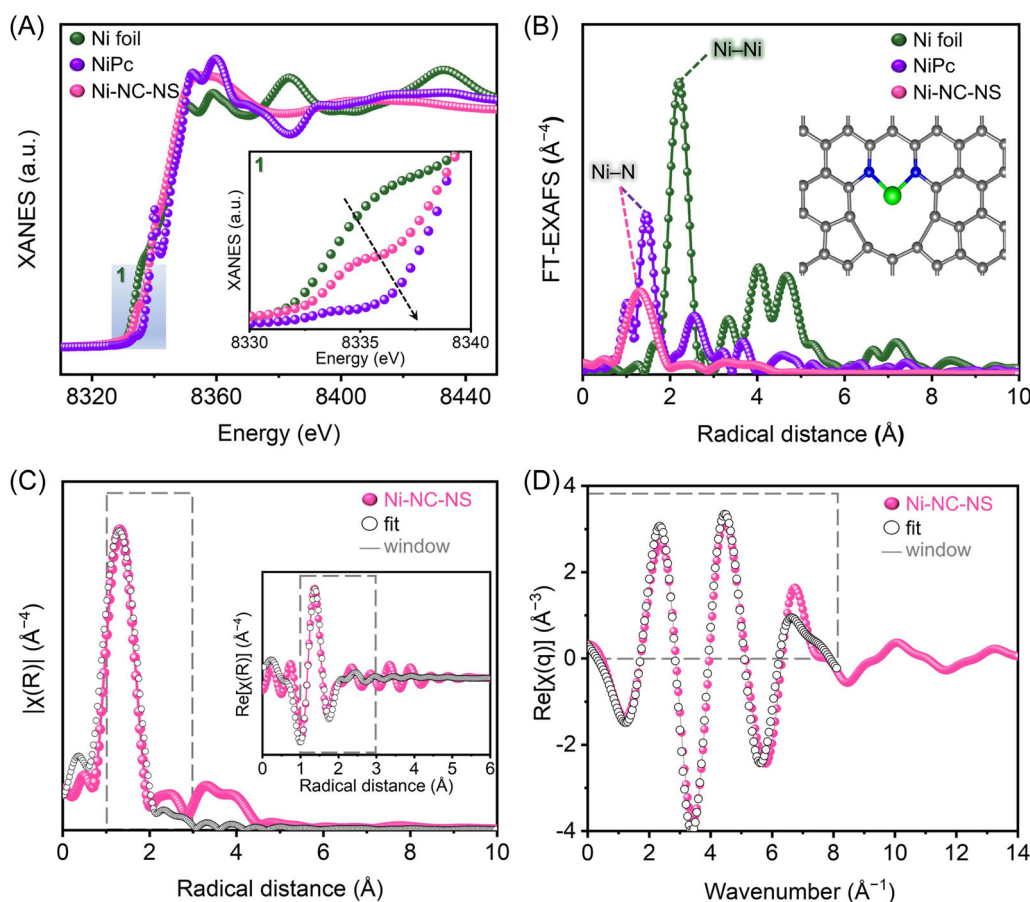


FIGURE 3 XAS analysis at the atomic level. (A) Ni K-edge XANES spectra (inset image is an enlargement of [A]), and (B) the k^3 -weighted FT-EXAFS spectra of Ni-NC-NS with Ni foil and NiPc as references. The proposed atomic structure of the Ni site in Ni-NC-NS is displayed in inset (B); gray, blue, and light-green balls represent the C, N, and Ni atoms, respectively. (C) Corresponding FT-EXAFS fitting curves in magnitude R space ($|\chi(R)|$), with inset showing FT-EXAFS fitting curves in real R space ($\text{Re}[\chi(R)]$), and (D) in real q space ($\text{Re}[\chi(q)]$) at the Ni K-edge for Ni-NC-NS.

materials and catalysts. The XAS data at the Zn K-edge of Ni-NC-P, which contained Zn, were compared to those of Ni-NC-NS, which did not contain Zn (Figure S17D-F and Table S4). XAS analysis revealed that Ni-NC-P exhibited a distinct combination of Ni-N and Zn-N interactions, whereas Ni-NC-NS predominantly characterized Ni-N interactions.

3.4 | Electrochemical CO₂RR performance in H-cell and flow-cell reactors

Based on the atomic environment findings, the electrocatalytic performance of the Ni-NC-NS catalyst, which features the NiN₂-V₂ interaction, was evaluated in the eCO₂RR. For this purpose, a conventional H-cell reactor with a 0.5 M KHCO₃ electrolyte was used, and its performance was compared with that of NC-NS, NC-P,

and Ni-NC-P. The H-cell was connected to an online GC system to quantitatively analyze the gas-phase products using a well-fitted calibration curve for gas standards (Figure S18). To stabilize the electrodes, representative chronoamperometric measurements of all the as-prepared samples were conducted over a range of potentials (Figure S19). The LSV polarization curves (Figure 4A) demonstrated that Ni-NC-NS achieved a significantly higher cathodic current in the potential range from -0.2 to -1.3 V versus RHE compared to NC-P, NC-NS, and Ni-NC-P, demonstrating superior electrocatalytic performance. Ni-NC-NS showed approximately 100% FE_{CO} under the potentials ranging from -0.7 to -1.0 V versus RHE and high CO partial current density (j_{CO}) of 18.1, 22.5, and 26.8 mA cm⁻² at -1.0, -1.1, and -1.2 V versus RHE, respectively. No liquid products were detected using ¹H NMR (Figure S20). The plots obtained using a TCD and FID for online GC detection at given potentials are represented in

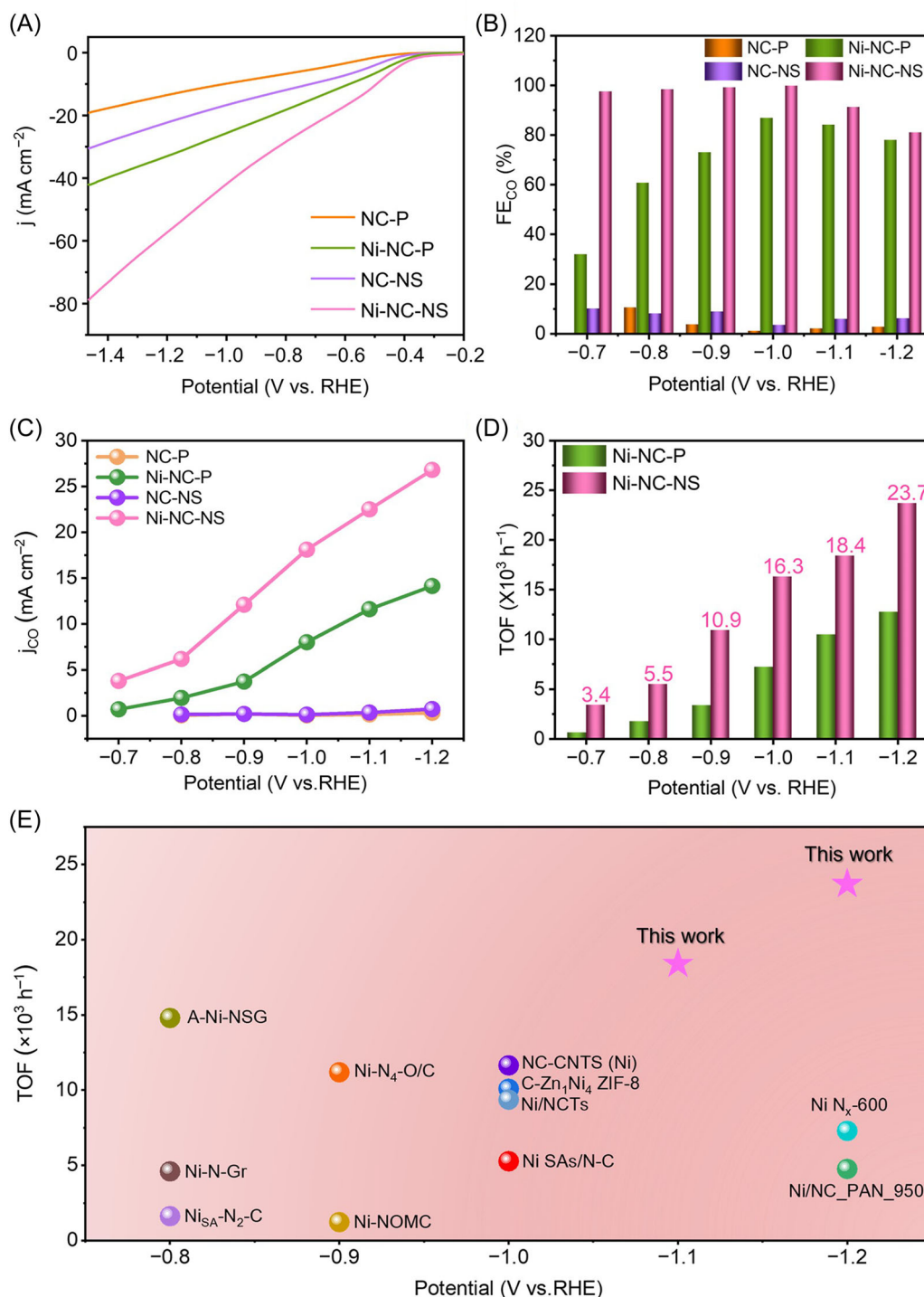


FIGURE 4 eCO₂RR performance of fabricated catalysts. (A) LSV polarization curves at a scan rate of 10 mV s⁻¹, (B) FE_{CO}, and (C) CO partial current density of Ni-NC-NS compared to those of NC-P, NC-NS, and Ni-NC-P in the potential range of -0.7 to -1.1 V versus RHE. (D) TOF values of Ni-NC-NS (Ni: 0.6 wt%) and Ni-NC-P (Ni: 1.21 wt%), which were derived from ICP-AES measurements (Table S1) at various applied potentials. All measurements were performed under the same conditions: CO₂-purged 0.5 M KHCO₃ and 20 mL min⁻¹ CO₂ flow. (E) Comparison of TOF values of reported Ni SAC-based eCO₂RR electrocatalysts in the H-cell reactor (TOF values of reported Ni SACs are arranged in Table S5). Our electrocatalysts are marked as pink stars.

Figure S21. Ni-NC-P exhibited an FE_{CO} of 86% at -1.0 V versus RHE and relatively lower j_{CO} than Ni-NC-NS (Figure 4B,C). Chronoamperometry measurements and FE for CO and H_2 on pristine carbon paper are shown in Figure S22 for an accurate comparison. The TOF was calculated using an electrode with Ni loading in the catalyst based on ICP-AES measurements to evaluate the intrinsic activity of the catalyst in an electrocatalytic system (Table S1).³² Ni-NC-NS exhibited an ultrahigh TOF value of $18,403\text{ h}^{-1}$ at -1.1 V versus RHE and $23,699\text{ h}^{-1}$ at -1.2 V versus RHE (Figure 4D), which are significantly higher than those of reported Ni SAC-based eCO_2RR catalysts under similar conditions (Figure 4E and Table S5). The smaller semicircle in the Nyquist plot of Ni-NC-NS indicated its faster charge-transfer capacity for CO formation than that of Ni-NC-P, owing to the lower interfacial resistance at the electrode/electrolyte interface, which facilitated the rapid catalytic kinetics of Ni-NC-NS toward CO formation (Figure S23A).⁹ A detailed explanation of the additional eCO_2RR performance of Ni-NC-NS, including the lowest Tafel slope (123 mV dec^{-1}), which favors the formation of the $COOH^*$ intermediate and a large ECSA to facilitate sufficient exposed active sites during the reaction, is shown in Figure S23B-H.^{33,34} Subsequently, 20, 40, and $60\text{ }\mu\text{L}$ of ink was deposited via the drop-casting method to investigate the impact of the amount of catalyst ink deposited on the carbon paper on the electrochemical performance (Figure S24A). Although FE_{CO} slightly decreased with increasing ink deposition, the Ni-NC-NS catalyst with $60\text{ }\mu\text{L}$ ink exhibited significantly high j_{CO} of 58.1 mA cm^{-2} and high FE_{CO} of 95.3% at -1.0 V versus RHE (Figure S24B-D). To evaluate the long-term stability of Ni-NC-NS, a constant chronoamperometry test was performed to resolve the limited stability of SACs. The performance decreased slightly compared to the initial test; however, high FE_{CO} and j_{CO} were maintained even after 10 h of long-term stability testing in the H-cell at -1.0 V versus RHE (Figure S25A). Single Ni atoms were inserted into the large specific surface area and abundant vacancy sites of the nanosheet; therefore, long-term stability could be obtained by interfering with Ni nanoparticle aggregation and efficiently suppressing hydrogen evolution.³⁵ After 10 h of stability testing, a negligible structural collapse was observed in the SEM and HAADF-STEM images (Figure S25B,C). Furthermore, XRD, XPS, and XAS revealed that the crystal structure and electronic state of Ni-NC-NS remained unchanged after an extended period of electrocatalytic stability testing, indicating the robust chemical stability of the catalyst (Figure S25D-G).

To enhance commercial viability by addressing the issue of limited CO_2 solubility in a conventional H-cell

reactor, a three-compartment microfluidic flow cell system was employed under ambient conditions (Figure 5A).³⁶ For cost-effectiveness, an optimal amount of catalyst ink (3 mg cm^{-2}) was deposited on a $1 \times 1\text{ cm}^2$ carbon paper substrate (Figure S26A). The LSV polarization curves of Ni-NC-NS in 0.5 M KHCO_3 and 1 M KOH electrolytes show a high cathodic current in the applied potential range from 0 to -1.2 V versus RHE (Figure S26B). The Ni-NC-NS in 0.5 M KHCO_3 electrolyte exhibits an excellent FE_{CO} of over 94% at a wide range of applied voltages from -0.8 to -1.2 V versus RHE and a j_{CO} of 114 mA cm^{-2} at -1.2 V versus RHE (Figure 5B,D). The eCO_2RR performance with an alkaline electrolyte (1 M KOH) recorded a significantly high j_{CO} of 210 mA cm^{-2} .³⁷ However, a slightly lower average FE_{CO} than that achieved in the 0.5 M KHCO_3 was observed (Figure 5C,E). We compared the recently reported Ni-SAC-based eCO_2RR catalysts used in flow cell reactors in terms of j_{CO} in two electrolyte environments (Figure S27).

3.5 | Theoretical study

A computational analysis using DFT calculations was performed to understand how vacancy sites in the atomic environment affect eCO_2RR activity. This study focused on the Ni-N-C active sites embedded in carbon support. Three models with varying vacancy sites, namely NiN_4 , NiN_3-V , and NiN_2-V_2 , were modeled around the isolated Ni sites (Figure 6A). The average Ni-N CNs of Ni-NC-P (3.2) and Ni-NC-NS (2.3) were obtained from the EXAFS results (Table S3). Based on these data, Ni-NC-P comprised the majority of NiN_3-V , with a small amount of NiN_4 . In contrast, Ni-NC-NS comprised the majority of NiN_2-V_2 , with a small amount of NiN_3-V . The DFT calculations revealed that the energy required for the desorption of CO^* to form $CO(g)$ on bare NiN_3-V and NiN_2-V_2 was markedly high, resulting in the formation of CO^* on the attached Ni sites (Figure S28). Therefore, the CO^* preadsorbed sites were used as the initial states for NiN_3-V and NiN_2-V_2 .³⁸ The first protonation step of CO_2 to form $COOH^*$ was the potential-determining step of NiN_4 ($\Delta G_{COOH^*} = 1.65\text{ eV}$), which resulted in improved catalytic activity (Figure 6B). Furthermore, a large number of vacancy sites in the porphyrin structure strengthened $COOH^*$ binding ($\Delta G_{COOH^*} = 0.93$ and 0.13 eV for single and double vacancy sites, respectively), thus facilitating a more positive limiting potential for the eCO_2RR ($U_L[CO_2]$; Figure 6C). Furthermore, this study investigated the effects of competitive HER. The vacancy sites strengthened H^* binding, leading to higher catalytic activity for the HER (Figure S29). This was likely due to

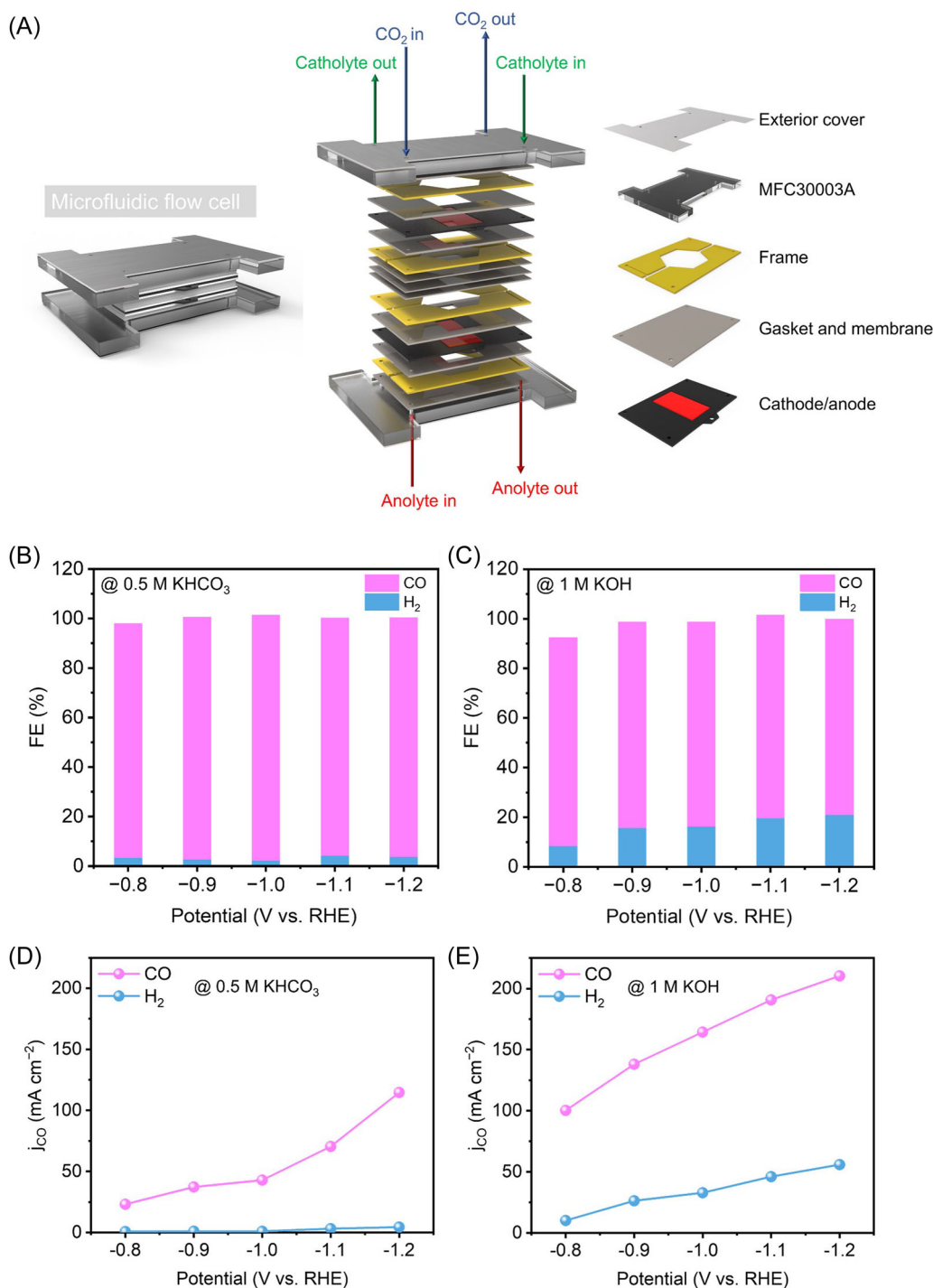


FIGURE 5 Flow cell assessments. (A) Schematic of a three-compartment microfluidic flow cell and its components. Faradaic efficiency for gas products and CO partial current density of Ni-NC-NS with 3 mg cm^{-2} (B, D) in CO₂-purged 0.5 M KHCO₃ and (C, E) in CO₂-purged 1 M KOH electrolytes at the applied potential range of -0.8 to -1.2 V versus RHE.

the scaling relationship between the C* and H* binding energies.³⁹ Both catalytic activity and selectivity were considered, and the values of $U_L(\text{CO}_2)$ and $U_L(\text{CO}_2) - U_L(\text{H}_2)$ were simultaneously evaluated. NiN₂-V₂ exhibits the most favorable $U_L(\text{CO}_2)$ and $U_L(\text{CO}_2) - U_L(\text{H}_2)$ values, surpassing those of NiN₄, implying that it is the

most promising catalyst for the eCO₂RR based on thermodynamic considerations. Microkinetic modeling confirmed that NiN₂-V₂ exhibited the highest TOF for the eCO₂RR to generate CO (Figure 6D).⁴⁰ This can be attributed to remarkably strong COOH* and moderate CO* binding, which enabled effortless CO₂ activation

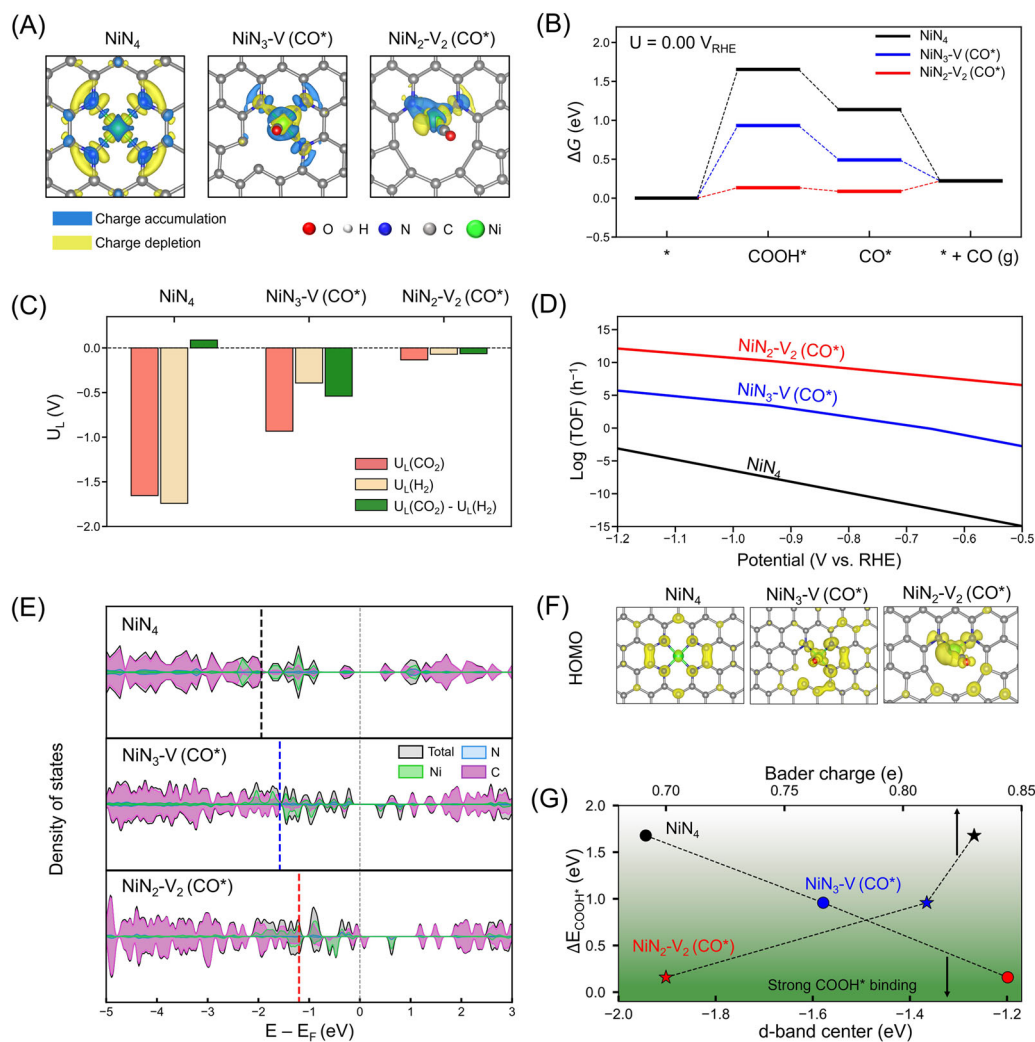


FIGURE 6 DFT calculations to unravel the mechanistic understanding. (A) Atomic structures of $\text{NiN}_x\text{-V}_y$ with charge density difference (CDD) plots, where (CO^*) indicates preadsorbed CO^* at the Ni sites. CDD is calculated as $\Delta\rho = \rho_{\text{total}} - \rho_{\text{Ni}} - \rho_{\text{N-NC}}$, where ρ_{total} , ρ_{Ni} , and $\rho_{\text{N-NC}}$ are charge densities of the total system, Ni metal site, and N-doped carbon support, respectively. The blue (yellow) area indicates charge accumulation (depletion), with an isosurface value of $0.04 \text{ e } \text{\AA}^{-3}$. (B) Gibbs free energy diagram of $\text{NiN}_x\text{-V}_y$. (C) The calculated limiting potentials (U_L) of $\text{NiN}_x\text{-V}_y$ under eCO_2RR and HER and their differences. More positive value of $U_L(\text{CO}_2) - U_L(\text{H}_2)$ indicates higher selectivity toward eCO_2RR . (D) The predicted TOF value using mean-field microkinetic modeling and (E) partial density of states of $\text{NiN}_x\text{-V}_y$ under eCO_2RR . The dashed vertical lines indicate the calculated d-band center values. (F) Electron density distributions of HOMO with an isosurface level set to $0.003 \text{ e } \text{\AA}^{-3}$. (G) Binding energies of COOH^* (y-axis) versus d-band center (lower x-axis) or Bader charge (upper x-axis). The color gradient indicates stronger COOH^* binding regions.

and CO desorption. Therefore, the computational analysis elucidated the exceptional catalytic activity of Ni-NC-NS observed in the electrocatalytic experiments based on the results obtained for $\text{NiN}_2\text{-V}_2$. For a more accurate comparison, the effect of residual Zn on Ni-NC-P was investigated. The ZnN_4 and $\text{ZnN}_3\text{-V}$ structures were modeled based on the EXAFS results, which showed an average CN of 3.6 (Table S4). DFT calculations indicated that the activation energy barriers for CO_2 to form COOH^* and the protonation of COOH^* to form CO^* were high for ZnN_4 and $\text{ZnN}_3\text{-V}$. Consequently, their catalytic activities were expected to

be lower than those of their Ni counterparts (Figure S30). This suggests that the facile removal of inactive Zn motifs from Ni-NC-NS contributes to its high catalytic activity and selectivity (Figure 2F-I). Electronic structure analyses were performed to investigate the effect of vacancy formation on the binding strength of the reaction intermediates. An upshift in the d-band centers relative to the Fermi level was observed, from -1.94 to -1.58 to -1.20 eV for NiN_4 , $\text{NiN}_3\text{-V}$, and $\text{NiN}_2\text{-V}_2$, respectively, with increasing vacancy sites (Figure 6E). Higher d-band center positions lead to less electron occupation of the antibonding states below the Fermi level, resulting in

stronger COOH* binding and easier activation of CO₂.⁴¹ These findings are supported by the Bader charge analysis,⁴² where the interaction between Ni sites and adsorbates strengthened with increasing vacancy sites as the number of Ni sites decreased (Figure 6A,G).^{43,44} As the vacancy sites increased, the highest occupied molecular orbital (HOMO) showed a more localized electron density near the Ni sites, facilitating electron donation for easier CO₂ activation and COOH* formation (Figure 6F).⁴⁵ These electronic structure analyses prove that introducing vacancy sites enhances the activity of the Ni sites in the eCO₂RR.

4 | CONCLUSION

An Ni SAC derived from a 2D nanosheet MOF was successfully fabricated by combining vacancy engineering and morphology reconstruction via solvent substitution. The abundant vacancy sites of Ni-NC-NS, detected using TGA, XRD, Raman spectroscopy, EPR, and theoretical studies, provided exposed sites, prevented metal aggregation, and stabilized the porphyrin structure. The Ni-NC-NS catalyst, comprising a single Ni atom combined with two nitrogen atoms and two vacancy sites confirmed using XAS, exhibited exceptional performance, with an FE_{CO} of approximately 100%, TOF of 23,699 h⁻¹, stability over 10 h in an H-cell reactor, and a remarkable *j*_{CO} of 210 mA cm⁻² in a three-compartment microfluidic flow cell reactor. Furthermore, DFT calculations provided significant insights into the vacancy effect and CO* preadsorbed states, which were used to investigate the most favorable atomic coordination environment for optimal performance of the eCO₂RR system.

ACKNOWLEDGMENTS

This research was conducted with financial support from the National Research Foundation of Korea (NRF), funded by the Korean government (2021R1A4A3027878, RS-2023-00209139). Additionally, support was received from the Korea Institute of Energy Technology & Energy (MOTIE) of the Republic of Korea (20212010100040). S. Back also acknowledges the support from the NRF, funded by the Ministry of Science and ICT (2015M3D3A1A01064929), and supercomputing time from KISTI.

CONFLICT OF INTEREST STATEMENT

The authors declare that there are no conflicts of interests.

ORCID

Ho Won Jang  <https://orcid.org/0000-0002-6952-7359>

Soo Young Kim  <https://orcid.org/0000-0002-0685-7991>

REFERENCES

- Sullivan I, Goryachev A, Digdaya IA, et al. Coupling electrochemical CO₂ conversion with CO₂ capture. *Nat Catal*. 2021;4(11):952-958.
- Galik CS. A continuing need to revisit BECCS and its potential. *Nat Clim Change*. 2020;10(1):2-3.
- McNutt M. Time's up, CO₂. *Science*. 2019;365(6452):411.
- Kim S, Kim KH, Oh C, Zhang K, Park JH. Artificial photosynthesis for high-value-added chemicals: old material, new opportunity. *Carbon Energy*. 2022;4(1):21-44.
- Nitopi S, Bertheussen E, Scott SB, et al. Progress and perspectives of electrochemical CO₂ reduction on copper in aqueous electrolyte. *Chem Rev*. 2019;119(12):7610-7672.
- Bagger A, Ju W, Varela AS, Strasser P, Rossmeisl J. Electrochemical CO₂ reduction: a classification problem. *Chemphyschem*. 2017;18(22):3266-3273.
- Jin B, Cho Y, Park C, et al. A two-photon tandem black phosphorus quantum dot-sensitized BiVO₄ photoanode for solar water splitting. *Energy Environ Sci*. 2022;15(2):672-679.
- Kim KH, Choi CW, Choung S, et al. Continuous oxygen vacancy gradient in TiO₂ photoelectrodes by a photoelectrochemical-driven "self-purification" process. *Adv Energy Mater*. 2022;12(7):2103495.
- Cho JH, Lee C, Hong SH, et al. Transition metal ion doping on ZIF-8 enhances the electrochemical CO₂ reduction reaction. *Adv Mater*. 2023;35:2208224.
- Wang X, Zhu Y, Li H, Lee J-M, Tang Y, Fu G. Rare-earth single-atom catalysts: a new frontier in photo/electrocatalysis. *Small Methods*. 2022;6(8):2200413.
- Kim J, Choi S, Cho J, Kim SY, Jang HW. Toward multicomponent single-atom catalysis for efficient electrochemical energy conversion. *ACS Mater Au*. 2022;2(1):1-20.
- Chen Y, Ji S, Chen C, Peng Q, Wang D, Li Y. Single-atom catalysts: synthetic strategies and electrochemical applications. *Joule*. 2018;2(7):1242-1264.
- Zhao C, Dai X, Yao T, et al. Ionic exchange of metal-organic frameworks to access single nickel sites for efficient electroreduction of CO₂. *J Am Chem Soc*. 2017;139(24):8078-8081.
- Wang Q, Ina T, Chen WT, et al. Evolution of Zn(II) single atom catalyst sites during the pyrolysis-induced transformation of ZIF-8 to N-doped carbons. *Sci Bull*. 2020;65(20):1743-1751.
- Song Z, Zhang L, Doyle-Davis K, Fu X, Luo JL, Sun X. Recent advances in MOF-derived single atom catalysts for electrochemical applications. *Adv Energy Mater*. 2020;10(38):2001561.
- Yin P, Yao T, Wu Y, et al. Single cobalt atoms with precise N-coordination as superior oxygen reduction reaction. *Angew Chem Int Ed*. 2016;55(36):10800-10805.
- Jia J, Xiong T, Zhao L, et al. Ultrathin N-doped Mo₂C nanosheets with exposed active sites as efficient electrocatalyst for hydrogen evolution reactions. *ACS Nano*. 2017;11(12):12509-12518.
- Jiang Y, Liu H, Tan X, et al. Monoclinic ZIF-8 nanosheet-derived 2D carbon nanosheets as sulfur immobilizer for high-performance lithium sulfur batteries. *ACS Appl Mater Interfaces*. 2017;9(30):25239-25249.
- Nozari V, Calahoo C, Tuffnell JM, Keen DA, Bennett TD, Wondraczek L. Ionic liquid facilitated melting of the metal-organic framework ZIF-8. *Nat Commun*. 2021;12:5703.

20. Seetharaj R, Vandana PV, Arya P, Mathew S. Dependence of solvents, pH, molar ratio and temperature in tuning metal organic framework architecture. *Arabian J Chem*. 2019;12(3): 295-315.
21. Wang Y, Mao J, Meng X, Yu L, Deng D, Bao X. Catalysis with two-dimensional materials confining single atoms: concept, design, and applications. *Chem Rev*. 2019;119(3):1806-1854.
22. Zhang H, Li Y, Zhao Y, Li G, Zhang F. Carbon black oxidized by air calcination for enhanced H₂O₂ generation and effective organics degradation. *ACS Appl Mater Interfaces*. 2019;11(31): 27846-27853.
23. Hong Z, Shen B, Chen Y, Lin B, Gao B. Enhancement of photocatalytic H₂ evolution over nitrogen-deficient graphitic carbon nitride. *J Mater Chem A*. 2013;1(38):11754-11761.
24. Eckmann A, Felten A, Mishchenko A, et al. Probing the nature of defects in graphene by Raman spectroscopy. *Nano Lett*. 2012;12(8):3925-3930.
25. Yang Z, Chen B, Chen W, et al. Directly transforming copper (I) oxide bulk into isolated single-atom copper sites catalyst through gas-transport approach. *Nat Commun*. 2019;10: 3734.
26. Yang HB, Hung SF, Liu S, et al. Atomically dispersed Ni(I) as the active site for electrochemical CO₂ reduction. *Nat Energy*. 2018;3(2):140-147.
27. Haase FT, Rabe A, Schmidt FP, et al. Role of nanoscale inhomogeneities in Co₂FeO₄ catalysts during the oxygen evolution reaction. *J Am Chem Soc*. 2022;144(27): 12007-12019.
28. Fan L, Xia C, Zhu P, Lu Y, Wang H. Electrochemical CO₂ reduction to high-concentration pure formic acid solutions in an all-solid-state reactor. *Nat Commun*. 2020;11:3633.
29. Avci C, Imaz I, Carné-Sánchez A, et al. Self-assembly of polyhedral metal-organic framework particles into three-dimensional ordered superstructures. *Nat Chem*. 2018;10(1): 78-84.
30. Gusmão R, Veselý M, Sofer Z. Recent developments on the single atom supported at 2D materials beyond graphene as catalysts. *ACS Catal*. 2020;10(16):9634-9648.
31. Chiarello GL, Ferri D. Modulated excitation extended X-ray absorption fine structure spectroscopy. *Phys Chem Chem Phys*. 2015;17(16):10579-10591.
32. Yan C, Li H, Ye Y, et al. Coordinatively unsaturated nickel-nitrogen sites towards selective and high-rate CO₂ electroreduction. *Energy Environ Sci*. 2018;11(5):1204-1210.
33. Lu Q, Rosen J, Zhou Y, et al. A selective and efficient electrocatalyst for carbon dioxide reduction. *Nat Commun*. 2014;5:3242.
34. Yang F, Elnabawy AO, Schimmenti R, et al. Bismuthene for highly efficient carbon dioxide electroreduction reaction. *Nat Commun*. 2020;11:1088.
35. Tekalgne MA, Do HH, Hasani A, et al. Two-dimensional materials and metal-organic frameworks for the CO₂ reduction reaction. *Mater Today Adv*. 2020;5:100038.
36. Liu W, Zhai P, Li A, et al. Electrochemical CO₂ reduction to ethylene by ultrathin CuO nanoplate arrays. *Nat Commun*. 2022;13:1877.
37. Gong Q, Ding P, Xu M, et al. Structural defects on converted bismuth oxide nanotubes enable highly active electrocatalysis of carbon dioxide reduction. *Nat Commun*. 2019;10:2807.
38. Ou L, He Z, Yang H, Chen Y. Theoretical insights into potential-dependent C-C bond formation mechanisms during CO₂ electroreduction into C₂ products on Cu(100) at simulated electrochemical interfaces. *ACS Omega*. 2021;6(28):17839-17847.
39. Back S, Yeom MS, Jung Y. Active sites of Au and Ag nanoparticle catalysts for CO₂ electroreduction to CO. *ACS Catal*. 2015;5(9):5089-5096.
40. Sa YJ, Jung H, Shin D, et al. Thermal transformation of molecular Ni²⁺-N₄ sites for enhanced CO₂ electroreduction activity. *ACS Catal*. 2020;10(19):10920-10931.
41. Nørskov JK, Abild-Pedersen F, Studt F, Bligaard T. Density functional theory in surface chemistry and catalysis. *Proc Natl Acad Sci*. 2011;108(3):937-943.
42. Tang W, Sanville E, Henkelman G. A grid-based bader analysis algorithm without lattice bias. *J Phys Condens Matter*. 2009;21(8):084204.
43. Cao S, Wei S, Wei X, et al. Can N, S cocomplexation promote single atom catalyst performance in CO₂RR? Fe-N₂S₂ porphyrin versus Fe-N₄ porphyrin. *Small*. 2021;17(29):2100949.
44. Yang Q, Xu W, Gong S, et al. Atomically dispersed Lewis acid sites boost 2-electron oxygen reduction activity of carbon-based catalysts. *Nat Commun*. 2020;11:5478.
45. Wang X, Jia Y, Mao X, et al. Edge-rich Fe-N₄ active sites in defective carbon for oxygen reduction catalysis. *Adv Mater*. 2020;32(16):2000966.

SUPPORTING INFORMATION

Additional supporting information can be found online in the Supporting Information section at the end of this article.

How to cite this article: Cho JH, Ma J, Lee C, et al. Crystallographically vacancy-induced MOF nanosheet as rational single-atom support for accelerating CO₂ electroreduction to CO. *Carbon Energy*. 2024;e510. doi:10.1002/cey2.510